Aerospace Science and Technology 96 (2020) 105535

Contents lists available at ScienceDirect

Aerospace Science and Technology

www.elsevier.com/locate/aescte

Effect of location of a transverse sonic jet on shock augmented mixing in a SCRAMJET engine

Vatsalya Sharma [a], Vinayak Eswaran [a,*,1], Debasis Chakraborty [b]

[a] Department of Mechanical and Aerospace Engineering, Indian Institute of Technology Hyderabad, India
[b] Directorate of Computational Dynamics, Defence Research and Development Lab, Hyderabad, India

ARTICLE INFO

Article history:
Received 4 September 2019
Received in revised form 2 November 2019
Accepted 2 November 2019
Available online 12 November 2019

Keywords:
SCRAMJET engine
RANS
Transverse sonic injection
Supersonic crossflow

ABSTRACT

Transverse sonic injection into supersonic cross flow is a well-established technique to inject fuel into a SCRAMJET combustor. A SCRAMJET combustor with a backward facing step acting as a flame-holder has been used for this study. The jet is placed at various locations downstream of the step, where each location represents a distinct flow region. Three-dimensional simulations have been performed using Menter's SST model in our in-house parallel 3-D RANS unstructured grid CFD solver. In such a SCRAMJET configuration, mixing between air and fuel is augmented by shocks generated by the under-expanded jet injected into the supersonic cross flow, hence the jet location is expected to be critical. The performance and mixing of the combustor has been quantified for each of the distinct configurations. The length of the combustor required for complete mixing has also been estimated for the different cases. It is observed that the mixing and performance are strongly affected by the location of the jet in the combustor flow-field. From the results presented in this paper, the optimal location for the jet is somewhat before the end of the recirculation region behind the backward facing step.

1. Introduction

Air-breathing engines are almost universally used in high speed aero-propulsion vehicles [1]. The SCRAMJET (supersonic ramjet) engine is an attractive candidate for very high speed (hypersonic) application due to its relatively simple design and its promise of delivering high thrust [2,3]. One of the challenges in the design of SCRAMJET engines is to ensure very rapid mixing between the air and fuel necessitated by the short residence time of the incoming air, which is of the order of several milliseconds for hypersonic flight conditions. Several methods to inject fuel into the incoming air have been investigated, both experimentally and computationally for mixing, combustion and ignition [1,4–9]. One of the methods studied is to inject the fuel in the transverse direction at sonic speed into the incoming supersonic air flow which results in a simple and reliable design [10–12].

Mixing of air and fuel in a combustor can be augmented by the presence of strong streamwise vorticity. The simplified (i.e., inviscid) equation for vorticity can be given as:

$$\rho \frac{D}{Dt}\left(\frac{\omega}{\rho}\right) = \frac{1}{\rho^2}\nabla\rho \times \nabla P \tag{1}$$

The baroclinic source term on the RHS of the Eqn. (1) shows that vorticity is generated in a fluid when the pressure and density gradients are non-parallel. When an under-expanded jet at sonic speed is injected in the transverse direction to the incoming flow, it creates a complex flow-field as described in detail by Sharma et al. [13]. The strong bow shock, created in the upstream region of the under-expanded jet, interacts with the fuel jet and creates a strong baroclinic torque. This augments mixing by creating strong streamwise vorticity in the flow field via the source term of Eqn. (1). However, this configuration also results in loss of stagnation pressure which directly leads to loss of thrust, resulting in a less efficient combustor design [10,14].

It is known that the baroclinic torque and the streamwise vorticity that are generated in the domain due to mixing are not significantly affected by the chemical kinetics and subsequent heat release in the flow field through combustion [15–17]. This results in the decoupling of the essential features of the flow from the combustion, and suggests that a cold flow analysis of the flow field could be used, at-least as a first approximation, to optimize the design of a SCRAMJET engine.

Another challenge in the design of a SCRAMJET combustor is to hold, sustain and stabilize the flame at very high speeds. Of the several configurations suggested by the researchers, a combustor

* Corresponding author.
E-mail address: eswar@iith.ac.in (V. Eswaran).
[1] Professor at MAE Department, IIT Hyderabad.

https://doi.org/10.1016/j.ast.2019.105535
1270-9638/

with injectors placed downstream of a backward facing step is one of the simplest designs capable of flame holding and stabilization [18–22]. The step creates a large recirculation zone which, with the hot gases contained therein, serves as a continuous ignition zone. The objective of this study is to establish an optimum distance of the leading fuel injector from the flame holder. There are several complex flow regions in the downstream of the backward facing step where the leading jet can be possibly placed in the combustor.

Experimental and numerical studies have been performed to investigate the role of the location of a transverse sonic jet in a supersonic crossflow with different configurations [23,14,24], but a detailed study analyzing the effect of the location of the injector on the overall performance of the SCRAMJET engine has not been published in the literature, and so is attempted in this work. A parallel three dimensional RANS based unstructured grid CFD solver has been recently developed in-house by the Sharma et al. [13] to solve all-speed compressible flow problems. This solver is used here for the three-dimensional numerical study of the SCRAMJET configurations, without combustion, to identify the optimal location of the leading jet.

In order to establish the optimal location, the jet is placed in different regions of the flow field downstream of the backward facing step, which creates distinct cases for study. The combustor design is then evaluated on the basis of better mixing of air-fuel and on other bases of performance. To quantify the mixing of fuel and air, we study the jet spread, penetration, effect of streamwise vorticity, and mixing efficiency. To quantify the performance of the SCRAMJET engine, the increase in entropy and stagnation pressure loss are evaluated and compared between the different cases. Using the data from the analysis, the combustor length required for complete mixing is also estimated. More than the mere numerical distance, emphasis has been laid on identifying the region where the leading jet should be placed, so as to find the common principle for different jet-to-free-stream pressure ratios.

2. Numerical method

The details of the in-house parallel three-dimensional unstructured grid RANS solver are given in this section.

2.1. Governing equation

The density based finite volume solver uses a low-speed preconditioned form of the Navier-Stokes equation [25] that allows its use for both the compressible and incompressible flow regimes. The solver can handle three-dimensional unstructured grids in CFD General Notification System (CGNS) format. The equation of state for an ideal gas is used:

$$p = \rho R T \tag{2}$$

where ρ, T, and P are the density, temperature and pressure of the fluid, respectively and R is the universal gas constant taken as 287 $\mathrm{J\,Kg^{-1}\,K^{-1}}$. The velocity vector is written as:

$$\mathbf{V} = u\hat{\mathbf{i}} + v\hat{\mathbf{j}} + w\hat{\mathbf{k}} \tag{3}$$

The integral form of the governing equation used, with control volume V and elemental face area $\mathbf{d}S$, is given as:

$$\Gamma \frac{\partial}{\partial t}\int_V \mathbf{Q}\,dV + \oint [\mathbf{F} - \mathbf{G}]\cdot d\mathbf{G} = \int_V \mathbf{H}\,dV \tag{4}$$

where $\mathbf{Q}$ is the primitive variables vector given as:

$$\mathbf{Q} = \{P, u, v, w, T\}^T \tag{5}$$

The magnitude of the face area $\mathbf{S}_f$ is A_f and its unit vector is $\hat{\mathbf{n}}_f$. In the governing equation (4), $\boldsymbol{G}$ is the diffusion vector and $\boldsymbol{F}$ is the convective vector of the compressible Navier-Stokes equation which are defined as:

$$\mathbf{F} = \begin{Bmatrix} \rho\mathbf{V} \\ \rho\mathbf{V}u + P\hat{\mathbf{i}} \\ \rho\mathbf{V}v + P\hat{\mathbf{j}} \\ \rho\mathbf{V}w + P\hat{\mathbf{k}} \\ \rho\mathbf{V}E + P\mathbf{V} \end{Bmatrix}, \quad \mathbf{G} = \begin{Bmatrix} 0 \\ \tau_{xi} \\ \tau_{yi} \\ \tau_{zi} \\ \tau_{ij}\mathbf{V}_j + \mathbf{q} \end{Bmatrix} \tag{6}$$

Here E and H are the total energy and total enthalpy per unit mass.

$$E = H - \frac{p}{\rho} \quad ; \quad H = h + |\mathbf{V}|^2/2 \tag{7}$$

and $\mathbf{q}$ is the heat flux vector:

$$\boldsymbol{q} = -k'\frac{\partial T}{\partial x_j} \tag{8}$$

where k' is the thermal conductivity of the fluid, and $\boldsymbol{\tau}$ is the viscous stress tensor:

$$\tau_{ij} = -P\delta_{ij} + \mu_L\left(\frac{\partial U_i}{\partial x_j} + \frac{\partial U_j}{\partial x_i}\right) + \lambda(div\mathbf{V})\delta_{ij} \tag{9}$$

where λ is the coefficient of bulk viscosity, determined using Stoke's hypothesis [26] and μ_L is the laminar dynamic viscosity of the fluid. In equation (4), Γ is the low speed preconditioning matrix that helps in getting accurate solutions for both compressible and incompressible flows for a density based algorithm [25]:

$$\Gamma = \begin{bmatrix} \Theta & 0 & 0 & 0 & \rho_T \\ \Theta u & \rho & 0 & 0 & \rho_T u \\ \Theta v & 0 & \rho & 0 & \rho_T u \\ \Theta w & 0 & 0 & \rho & \rho_T u \\ \Theta H - \delta & \rho u & \rho v & \rho w & \rho_T H + \rho C_p \end{bmatrix} \tag{10}$$

where,

$$\Theta = \left(\frac{1}{U_r^2} - \frac{\rho_T}{\rho C_p}\right), \quad \rho_p = \left.\frac{\partial\rho}{\partial P}\right|_T, \quad \rho_T = \left.\frac{\partial\rho}{\partial T}\right|_P \tag{11}$$

In equation (11), U_r is the reference velocity and δ is a constant of preconditioning, whose definitions can be found in Weiss et al. [27]. The vector $\boldsymbol{H}$ in the equation (4) contains source terms for body forces and energy sources, which have been set as 0 in this work. The 2nd order Roe scheme [28], preconditioned for low speeds [27] has been used for modeling the convective vector $\boldsymbol{F}$ of the governing equation with the Venkatkrishnan limiter [29,30]. The gradients in the diffusion vector $\boldsymbol{G}$ are computed using the Green-Gauss cell based method.

Explicit time-stepping is used to march the solution to steady-state using the 4th order Runge Kutta method on the governing equations. The time step Δt is computed from the CFL (Courant-Friedrichs-Lewy) condition. The same time step Δt is used in each cell of the domain. The residue e of each variable solved is stored and is checked for convergence independently:

$$e = \sqrt{\frac{1}{\Delta t}\sum_{cells}\left(\mathbf{Q}^{n+1} - \mathbf{Q}^{n}\right)} \tag{12}$$

Normalization with the initial residual is used to ensure that the initial residuals for all equations are of $O(1)$, which is quite useful in judging overall convergence. Further details of the method and the equations can be found in Sharma et al. [13].

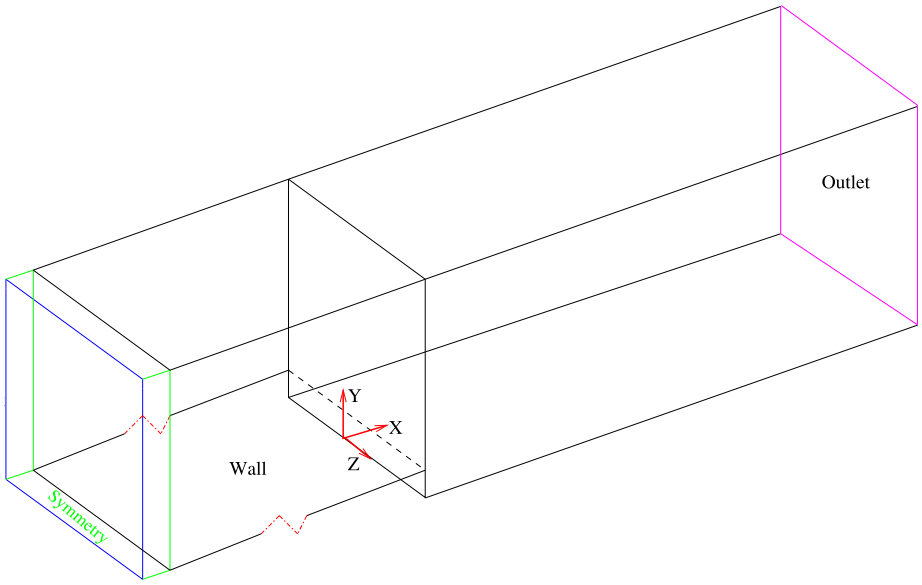

Fig. 1. Isometric view of the domain.

2.2. Turbulence modeling

The performance of various turbulence models for analyzing the interaction of transverse sonic jet in supersonic cross-flow has been evaluated by researchers [31,32,13] in the literature. Based on these results, for the given flow conditions the SST k-ω two-equation model by Menter [33] can be expected to give good results. Therefore, the SST k-ω two-equation model by Menter [33] in its low Reynolds number form is used in this study. The model equations are:

$$\frac{\partial(\rho k)}{\partial t} + \frac{\partial(\rho U_j k)}{\partial x_j} = P_k - \beta^* \rho \omega k + D_k \tag{13}$$

$$\frac{\partial(\rho \omega)}{\partial t} + \frac{\partial(\rho U_j \omega)}{\partial x_j} = \gamma' \frac{\omega}{k} P_k - \beta \rho \omega^2 + D_\omega + AA \tag{14}$$

where P_k is the production of turbulent kinetic energy evaluated as:

$$P_k = \tau_{ij} \frac{\partial U_j}{\partial x_i} \tag{15}$$

The rest of the model constants and definitions are as given by Menter [33]. The value of the laminar Prandtl number is taken as 0.71 and the turbulent Prandtl number (Pr_T) is taken as 0.9.

2.3. Passive scalar tracking to determine mixing

A convection-diffusion equation is also solved coupled with the system of governing equations in order to track mixing of the injected jet with the main air flow. For a passive scalar ϕ, the governing equation can be given as:

$$\frac{\partial \rho \phi}{\partial t} + \frac{\partial}{\partial x_i}(\rho \phi u_i) - \frac{\partial}{\partial x_i}\left(\rho \Gamma \frac{\partial}{\partial x_i}\phi\right) = S_\phi \tag{16}$$

where ρ is the density of the fluid, u_i is the component of the fluid velocity vector V and S_ϕ is the source term (which is set as 0 here), and Γ is the diffusivity for the scalar, given as:

$$\Gamma = \Gamma_k + \Gamma_t \tag{17}$$

where Γ_k is the molecular diffusivity where value is taken equal to the kinematic viscosity of the fluid, while the turbulent eddy diffusivity Γ_t is evaluated as:

Table 1
Domain dimensions.

Parameter	Value
Height of step (H)	3.184 mm
Section height (H_1)	$6.68H$
Section width (W)	$9.57H$
Step location	$\frac{X}{H} = 0.0$
L_1	$34.0H$
L_2	$19.0H$
L_s	$1.0H$

$$\Gamma_t = \frac{\mu_t}{Sc_t} \tag{18}$$

where μ_t is turbulent viscosity obtained from the solver, and the value of turbulent Schmidt number (Sc_t) is taken as 0.9.

The scalar ϕ is the "*mixing fraction*" that is given the value of 1 in the fuel jet stream and 0 in the air inlet stream. As the fuel stream and air stream mix we will get values of ϕ between 0 and 1. The value of ϕ at a point in the flow will indicate the amount of mixing of the fuel and air streams, with $\phi = 1$ indicating unmixed fuel steam and 0 unmixed air stream and, say $\phi = 0.4$ indicating a 40% fuel stream and 60% air stream mixture (by mass). In practice, the fuel stream would be say, a kerosene-air mixture, which for convenience we take in this study to have the same and properties as air.

3. Numerical validation and verification of the solver

The RANS solver is validated for benchmark cases to establish its capabilities and accuracy in the following sub-sections.

3.1. Supersonic turbulent flow over backward facing step

Turbulent supersonic flow of Mach Number (M_∞) 2.05 is computed over a confined backward facing step and is compared against the experimental results of McDaniel et al. [19]. Fig. 1 shows the isometric view of the 3-D computational domain. The X-Y plane view of the domain is shown in Fig. 2. In both figures the length L_1 is shown shortened (as indicated by the line break). The dimensions of the domain are given in Table 1. As SST is a low Reynold's number model, $y^+ < 1$ is required for the first grid point near the wall. The grid is stretched in the wall-normal direction,

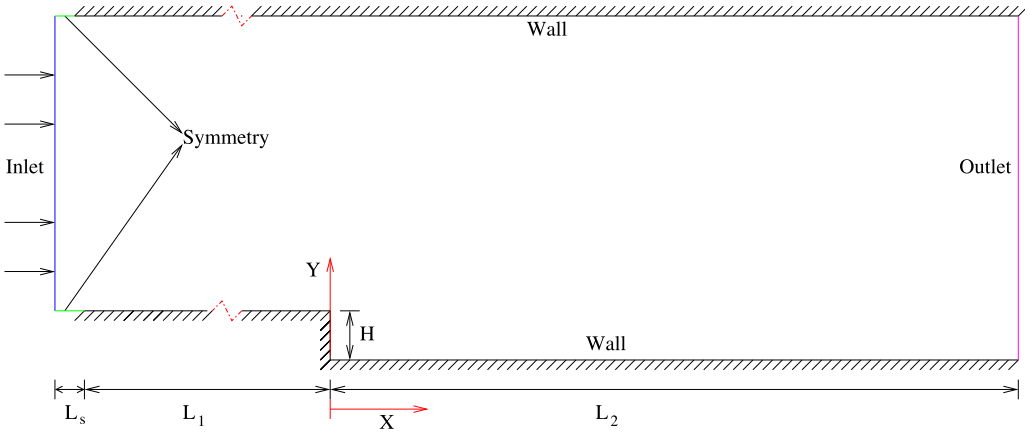

Fig. 2. Geometry for simulations and its boundary conditions.

Table 2
Boundary conditions for turbulence variables.

Section name	SST boundary condition
Inlet	$I = 5\%$
Adiabatic Wall	$k = 0\ \omega = 0$
Outlet	$\frac{\partial k}{\partial n} = 0\ \frac{\partial \omega}{\partial n} = 0$
Symmetry	$\frac{\partial k}{\partial n} = 0\ \frac{\partial \omega}{\partial n} = 0$

and is also clustered near the plate's leading edge. A hyperbolic law is used to distribute the nodes in the Y direction so as to have more nodes near the wall. Uniform node distribution is used in the X and Z directions.

At the inlet, pressure inlet boundary conditions have been prescribed, with a total pressure (P_t) of 274000 Pa, static temperature (T_{static}) = 167 K and a total Temperature (T_t) of 250 K. The wall is assumed as adiabatic, where $\mathbf{U} = 0$, $\frac{\partial T}{\partial n} = 0$, $\frac{\partial P}{\partial n} = 0$, $\frac{\partial \tilde{\nu}}{\partial n} = 0$ have been prescribed as boundary conditions. At the exit, outflow boundary condition have been prescribed. Symmetry conditions are prescribed at the Z direction boundaries. For all the sections labeled as symmetry, $\frac{\partial \mathbf{Q}}{\partial n} = 0$ has been prescribed, where $\mathbf{Q} = \{p, u, v, w, T\}^T$. The boundary conditions for the various turbulent quantities has been given in Table 2. For calculating the value of the turbulent kinetic energy k and the turbulent energy dissipation rate ϵ at the inlet, the value of turbulence intensity (I) is used in the following formulae:

$$k = 1.5 I^2 U_{inlet}^2 \tag{19}$$

$$\epsilon = C_\mu^{3/4} K^{3/2} l^{-1} \tag{20}$$

and the specific dissipation rate ω is obtained as:

$$\omega = \frac{K}{C_\mu \epsilon} \tag{21}$$

where U_{inlet} is the inlet velocity, l is the turbulence integral length scale specified as $l = 0.07L$, where L is the characteristic length of domain, and has been taken as the height of the step. The value of I is taken as 5%(= 0.05). The solution is computed using 4th order Runge Kutta explicit time stepping with CFL numbers ranging between $0.1 - 0.5$. We checked that the same result is obtained for all the aforementioned CFL numbers, showing a good temporal convergence. The solution is considered converged once the velocity and pressure residuals are below $1e^{-6}$ and turbulent variables' residuals are below $1e^{-3}$.

Table 3
Table showing grid convergence index (GCI) study.

Parameter	Value
N_1, N_2, N_3	3256500, 399822, 48291
r_{21}	2.008
r_{32}	2.015
ϕ_1	3.7019
ϕ_2	3.5936
ϕ_3	3.4695
p	1.784
ϕ_{ext}^{21}	3.7458
e_a^{21}	2.92%
GCI^{21}	1.48%
e_a^{32}	10.46%
GCI^{32}	5.34%

3.1.1. Grid convergence index

A grid sensitivity study was done with three grids with $N_1 = 3256500$, $N_2 = 399822$ and $N_3 = 48291$ grid points respectively, using the Grid Convergence Index (GCI) [34]. The results obtained with these grids have been tabulated in Table 3. The parameter used for GCI is the length of the recirculation zone (L_r), that has been referred to as ϕ in the Table 3. In Table 3, N is the number of elements in each mesh, $r = \sqrt{\frac{N_{coarse}}{N_{fine}}}$, p is the apparent order of calculation. As $N1 > N2 > N3$, e_a^{21} represents the approximate relative error and GCI_{21} is the fine grid convergence index, which gives the uncertainty in the value of the result on the finest mesh. On the basis of GCI, the 3-D grid with 3256500 hexahedral cells, with uncertainity of 1.48% is selected for the further computations. In order to compare the results with the experiments of McDaniel et al. [19], the pressure, velocity-X and temperature are normalized with respect to the free-stream values, as follows:

$$P_{norm} = \frac{P}{P_\infty} \tag{22}$$

$$U_{norm} = \frac{U_x}{U_{x,\infty}} \tag{23}$$

$$T_{norm} = \frac{T}{T_\infty} \tag{24}$$

and

$$Y_{norm} = \frac{Y}{Y_{max}} \tag{25}$$

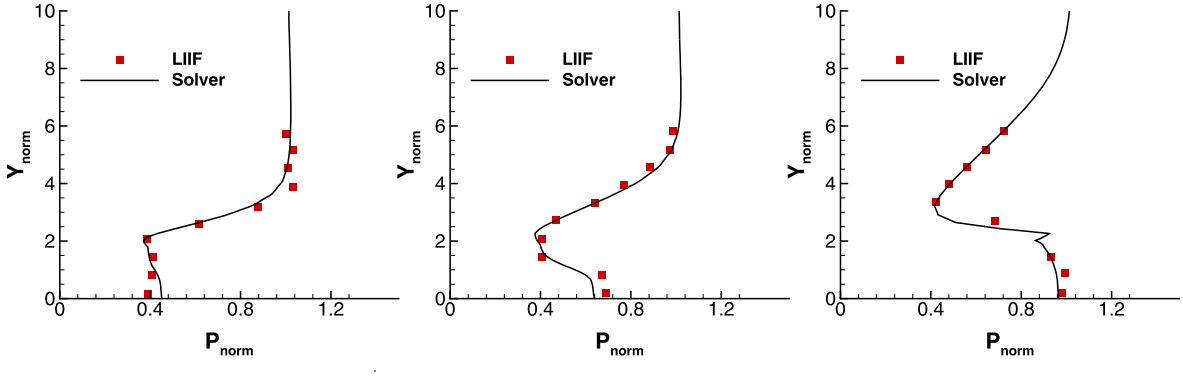

(a) $X/H = 1.48$ (b) $X/H = 3.0$ (c) $X/H = 7.0$

Fig. 3. Comparison of the center-plane P_{norm} profile at different X/H against LIFF experiments done by McDaniel et al. [19].

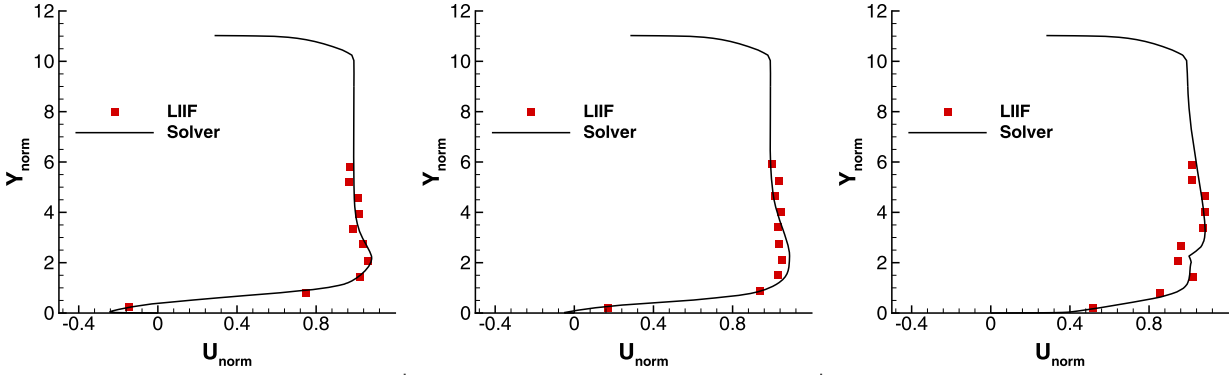

(a) $X/H = 1.48$ (b) $X/H = 3.0$ (c) $X/H = 7.0$

Fig. 4. Comparison of the center-plane U_{norm} profile at different X/H against experiments done by McDaniel et al. [19].

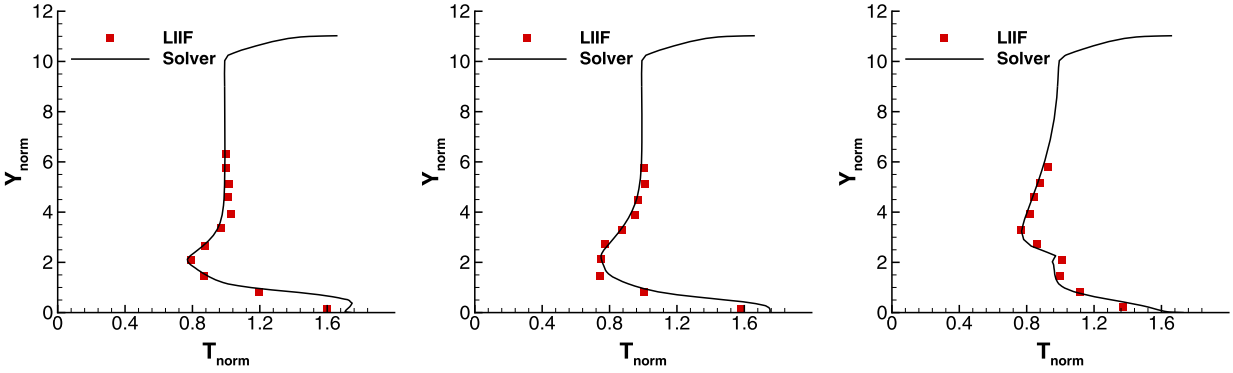

(a) $X/H = 1.48$ (b) $X/H = 3.0$ (c) $X/H = 7.0$

Fig. 5. Comparison of the center-plane T_{norm} profile at different X/H against LIFF experiments done by McDaniel et al. [19].

The computed results are then compared against the experimental Laser Induced Iodine Fluorescence (LIIF) values of P_{norm}, U_{norm} and T_{norm} as shown in Fig. 3, 4 and 5 respectively, for different locations at the mid X-Y plane. It can be seen that a good match is obtained for all the quantities.

3.1.2. Physical description of the supersonic flow over a backward facing step

Although this case has been used merely for the validation of the solver, it is interesting to review the physical features of the flow as we will see similar flow structures (plus some more) in our actual study. The fully developed supersonic turbulent flow encounters the sharp backward facing step that separates the turbulent boundary layer leading to the formation of a shear layer. The flow below this shear layer is slower than the fluid above it. This separated shear layer then curves downwards to subsequently impinge on the bottom wall, forming a recirculation zone below the shear layer. The turning of the flow at the step leads to the formation of multiple expansion waves known as the Prandtl Meyer Expansion Fan (PMEF) as seen in Fig. 6. Fig. 6 also shows the P_{norm} isobars to give an overview of the shocks in the flow domain. It also shows the streamlines in the region near the step marking the extent of the recirculation and the reattachment stagnation point. Within this recirculation region, a smaller recirculation with an opposite rotational sense can be seen in Fig. 6 at the lower corner of the step. The Figs. 3a, 4a and 5a show the qualitative features

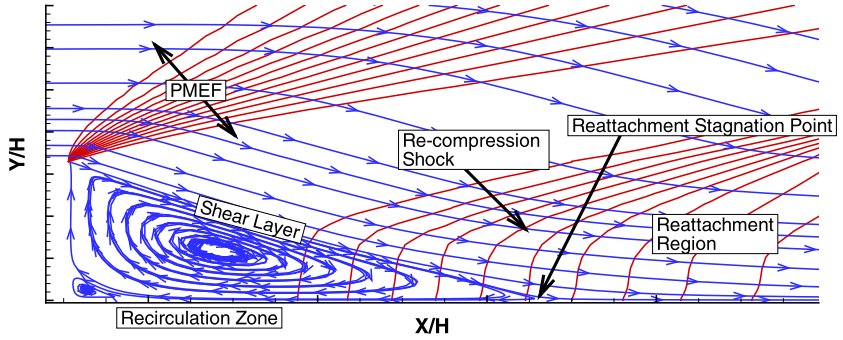

Fig. 6. X-Y plane view of flow around the step showing flow field with P_{norm} isobars mapped alongside velocity streamlines.

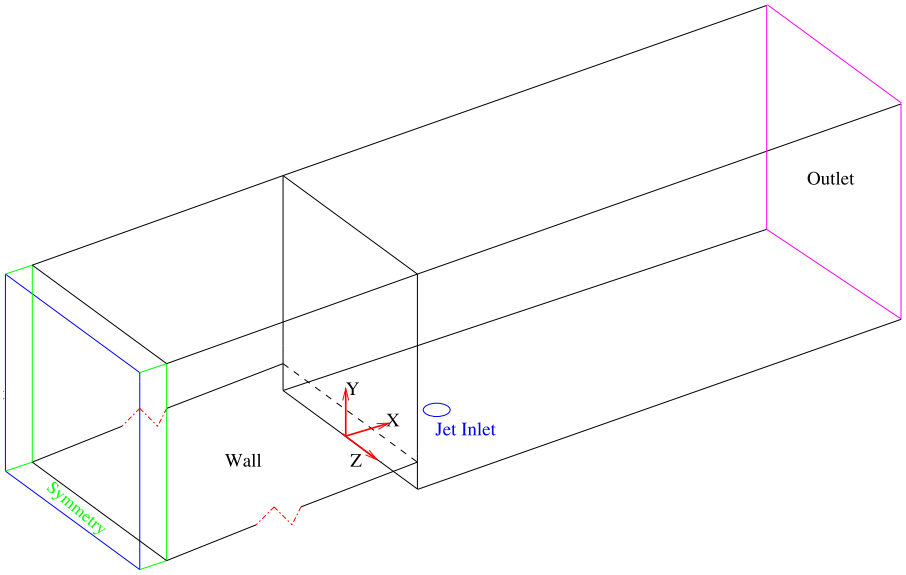

Fig. 7. Isometric view of the domain.

of the flow in the recirculation zone. The characteristics of a free shear layer persist outside this zone. The flow then reattaches itself to the wall at the reattachment stagnation point, passing through a series of reattachment shocks, as seen in Fig. 6, that re-normalize the pressure ratio to 1. In the post reattachment region, a boundary layer develops at the lower wall surface.

3.2. Transverse sonic injection in supersonic cross flow over backward facing step

We now consider another validation case for the solver and the turbulence model. Experiments using Laser Induced Iodine Fluorescence (LIIF) were done by McDaniel et al. [18] to study the penetration and spread of a single transverse sonic jet in a supersonic cross flow over a backward facing step. This data is now used to further validate our solver. A 3-D isometric view of the computational domain, along with boundary section names, is shown in Fig. 7. Fig. 8 shows the 2-D views in the planes parallel and normal to the injectors. The required dimensions are given in Table 4.

Meshes are made using the ICEM-CFD software in CGNS format. Unstructured 3-D meshes with quadrilateral elements at the boundary section and hexahedral elements in the inner computational section have been used. Fig. 9 shows the mesh distribution in the computational domain.

In order to optimize the number of cells in the mesh, hyperbolic and exponential laws for node distribution have been used at different sections. Nodes are clustered near the leading edge of the inlet section. After the simulation, it is checked that $y^+ < 1$, as required, for the grid points nearest to the wall. The grid is stretched in the wall-normal direction using the hyperbolic law as seen in Fig. 9a. The grid is clustered selectively at the jet inlet as shown in Fig. 9b, using the hyperbolic mesh law to capture the important flow features. Fig. 9c shows the exponential mesh distribution used in the Z direction. A symmetry boundary condition is prescribed on the boundary plane in the Z direction. At least 30% of the nodes in transverse direction are concentrated near the walls within a distance equal to three times the diameter of the injector.

Table 4
Domain dimensions.

Parameter	Value
Injector Diameter (D)	1.93 mm
Injector Location	$\frac{X}{D} = 0.0$
L_1	$\frac{X}{D} = 56.0$
L_2	$\frac{X}{D} = 31.0$
L_3	$\frac{X}{D} = 4.94$
W	$\frac{X}{D} = 31.0$
H	$\frac{X}{D} = 15.8$
Step location	$\frac{X}{D} = -4.94$

At the inlet, for a free-stream Mach number (M_∞) of 2.05, pressure inlet boundary conditions have been prescribed with total pressure (P_t) = 274000 Pa, static temperature (T_{static}) = 163 K and total temperature (T_t) of 250 K. The walls are assumed as adi-

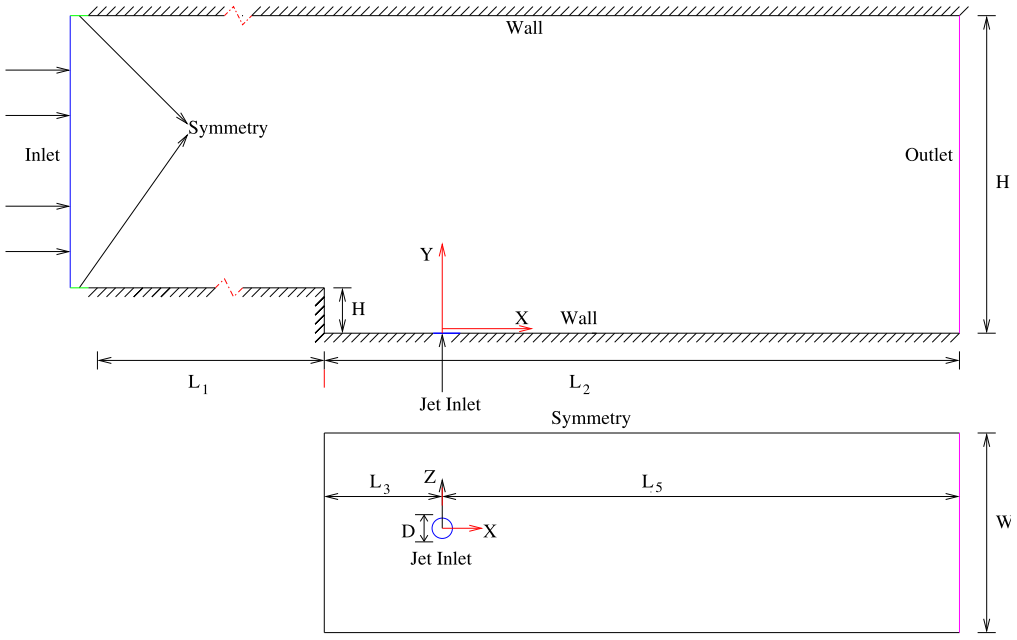

Fig. 8. Geometry for simulations and its boundary conditions.

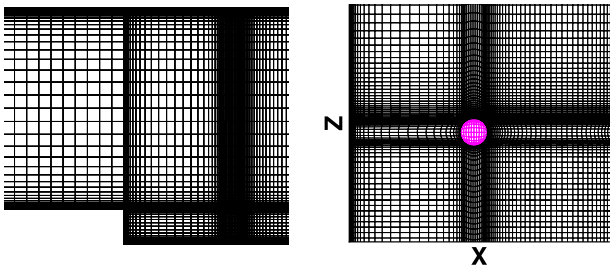

(a) Mesh distribution in the domain in X-Y plane

(b) Mesh distribution around the injector.

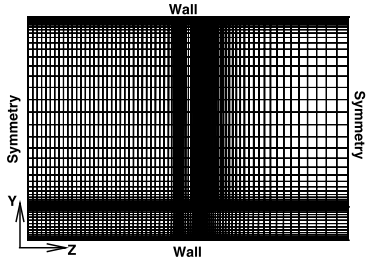

(c) Meshing in Y-Z plane as seen from the outlet section.

Fig. 9. Mesh distribution.

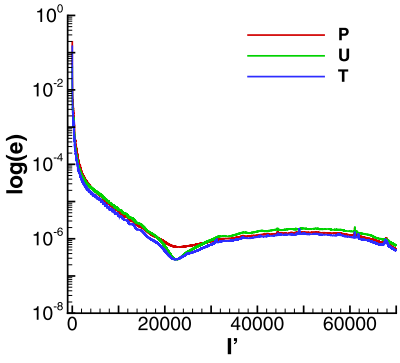

Fig. 10. Convergence history of primitive variables. (For interpretation of the colors in the figure(s), the reader is referred to the web version of this article.)

Table 5
Boundary conditions for turbulence variables and passive scalar.

Section name	SST boundary condition	Scalar (ϕ) boundary conditions
Inlet	$I = 5\%$	$\phi = 0$
Adiabatic Wall	$k = 0$ $\omega = 0$	$\phi = 0$
Outlet	$\frac{\partial k}{\partial n} = 0$ $\frac{\partial \omega}{\partial n} = 0$	$\frac{\partial \phi}{\partial n} = 0$
Symmetry	$\frac{\partial k}{\partial n} = 0$ $\frac{\partial \omega}{\partial n} = 0$	$\frac{\partial \phi}{\partial n} = 0$
Transverse Jet Inlet	$\frac{\partial k}{\partial n} = 0$ $\frac{\partial \omega}{\partial n} = 0$	$\phi = 1$

abatic, so $\mathbf{U} = 0$, $\frac{\partial T}{\partial n} = 0$, $\frac{\partial P}{\partial n} = 0$, $\frac{\partial \tilde{\nu}}{\partial n} = 0$ have been prescribed as boundary conditions there. At outflow, $\frac{P_t}{P_\infty} = 1$ has been prescribed, with the remaining quantities taken from interior values. Symmetry boundary conditions are prescribed in the Z direction planes. For all the sections labeled as symmetry, $\frac{\partial \mathbf{Q}}{\partial n} = 0$ has been prescribed. Since the injection is done at sonic speed, choked flow conditions are prescribed at the jet inlet. The inlet jet dynamic pressure ratio (Q) is given as:

$$Q = \frac{1}{M_\infty^2} \frac{P_{jet}}{P_\infty} \tag{26}$$

where P_{jet} is the injected jet static pressure and P_∞ is the free stream static pressure. Simulations were performed for $Q = 0.36$ and 0.75 corresponding to the experimental results of McDaniel et al. [18]. The jet is tracked using a passive scalar as described in Sec. 2.1. Boundary conditions for the turbulent variables and for the passive scalar are given in Table 5. Explicit time stepping using the Runge-Kutta 4th order scheme as described in Sharma et al. [13] with CFL number ranging between $0.1 - 0.3$ are used for the simulation. The solution is considered converged once the velocity, pressure and temperature residuals are below $1e^{-6}$ and turbulent variables' residuals are below $1e^{-3}$ (see Fig. 10). This convergence criteria shall be used for all the cases in the paper. The jet penetra-

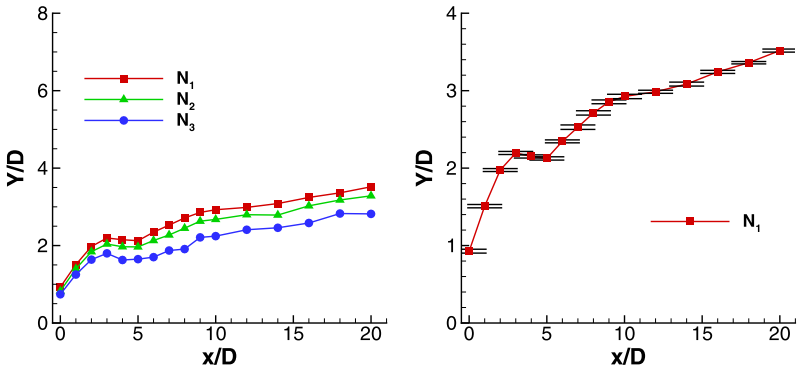

(a) Comparison of jet penetration results on different grids

(b) Jet penetration at the finest grid with error bars

Fig. 11. Results from Grid Convergence Index (GCI) study.

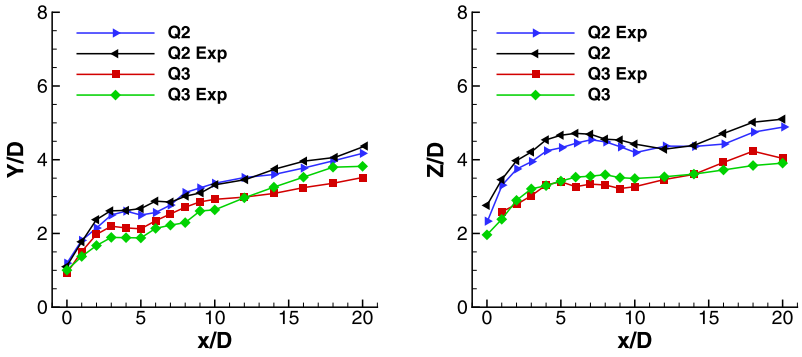

(a) Jet penetration

(b) Jet Spread

Fig. 12. Comparison of jet penetration and spread against experiments done by McDaniel et al. [18] on the finest grid.

tion and spread is measured using the value of the passive scalar (ϕ). The jet penetration is obtained by extracting the contour of $\phi = 1\%$ on the X-Y mid plane of the domain. The jet spread is obtained by extracting the same contour of $\phi = 1\%$ at the Y-Z plane located at a distance D from the injector.

3.2.1. Grid independence study

A grid sensitivity study was done with three grids of size $N_1 = 3256500$, $N_2 = 399822$ and $N_3 = 48291$ respectively, using the Grid Convergence Index (GCI) [34]. Fig. 11 shows the comparison of the penetration for Q = 0.75 using these three grids. On the finest grid, the estimated order of accuracy p_{avg} was obtained as 1.612 and the maximum GCI was obtained as 2.44%. Fig. 11b shows the penetration on the finest grid along with GCI error bars. Hence, the 3-D grid with 3256500 hexahedral cells is selected for the further computations. Using this grid, the jet penetration and spread is compared against the experimental results of McDaniel [18] as shown in Fig. 12 for Q = 0.75 and 0.25, respectively, named as Q_2 and Q_3 in the figure. A good match is seen to be obtained.

4. Results

The results presented in Sec. 3.1 and 3.2 give us some idea of the flow field that exists in the SCRAMJET engine. It can be seen that the turbulent supersonic flow over a backward facing step creates various complex flow regions that substantially differ from each other.

The results from Sec. 3.2 show that the penetration and spread of a transverse sonic injection depends on the dynamic pressure ratio. As seen in Sec. 3.1, especially in Fig. 6, the flow-field near the bottom wall has:

1. A Recirculation region.
2. A Reattachment Stagnation point.
3. A Reattached region.

For the case simulated, the reattachment point is located at $\frac{X}{H} = 3.13$. In order to determine an optimal location for the injector, it is now placed in or at the three aforementioned locations, each creating a distinct case of numerical simulation. The computational domain shown in Fig. 8 is used for the study. The length L_3 in Fig. 8 represents the distance of the center point of the injector from the step. This length for each of the distinct numerical case is as follows:

1. Case A - Inside the recirculation region at $X/H = 2.5$.
2. Case B - At the stagnation point $X/H = 3$.
3. Case C - In the reattachment region at $X/H = 8.5$.

In order to make comparison more reader friendly, and to make the injector as the reference point for all further comparisons, the origin for all the simulations has been shifted to the center of the injector inlet, the streamwise distance from which is given by x (in lowercase), and all the dimensions have been normalized with injector diameter D. Hence, the position of the origin is as follows for the three cases:

1. Case A - $x/D = 0$ at $X/H = 2.5$.
2. Case B - $x/D = 0$ at $X/H = 3$.
3. Case C - $x/D = 0$ at $X/H = 8.5$.

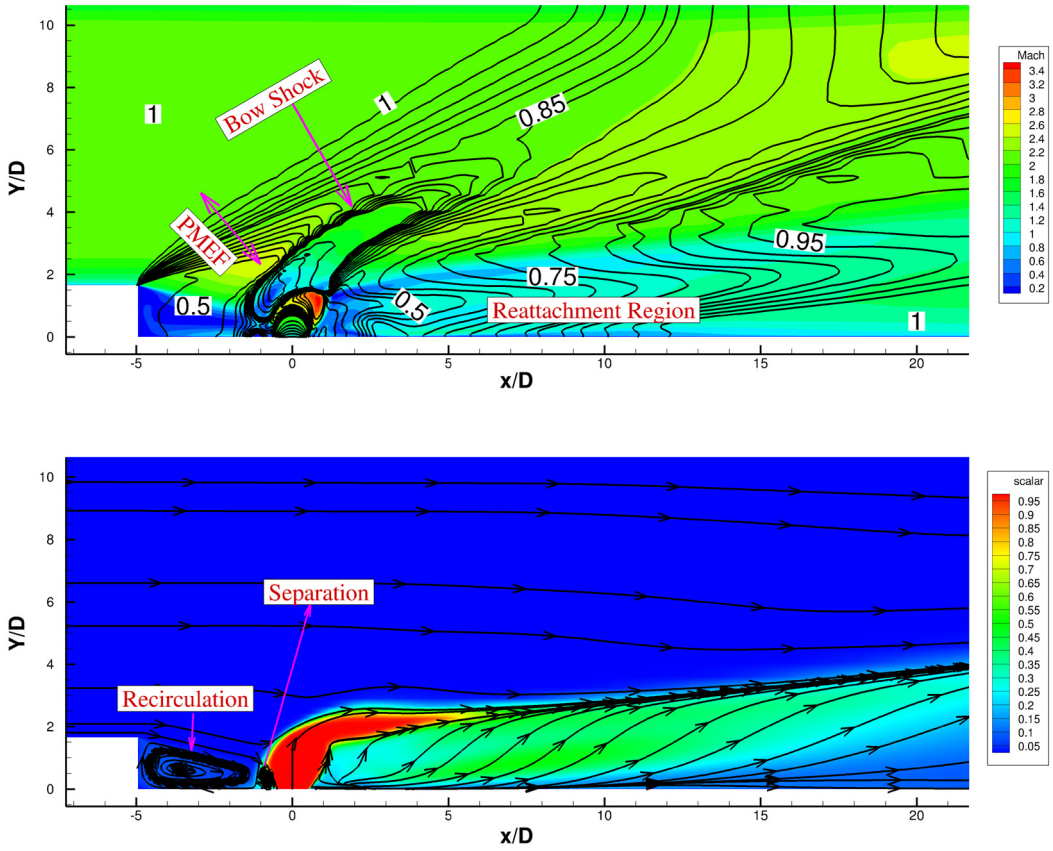

Fig. 13. Top: Center-plane P_{norm} isobars with Mach number contours. Bottom: Mass fraction of scalar with stream lines.

The number of nodes on L_3 and L_5 are redistributed for each of the 3 cases in order to keep the total number of cells, constant across all the cases. The local distribution of nodes around the injector and for the remaining directions is maintained the same as stated in Sec. 3.2. The total mesh size for each case is 3256500 hexahedral cells. The mesh, and the convergence criteria explained in Sec. 3.2 has been used for all the cases.

4.0.1. Overview of the flow field

Fig. 13 shows the key features of the flow field created by injecting a transverse sonic jet in the supersonic cross flow in the SCRAMJET combustor. The figure consists of two parts. In the first part, the P_{norm} isobars with Mach number contours have been plotted, whereas in the lower part, the contours mixing fraction of injected scalar with streamlines are shown. The plots are of the mid-X-Y plane of the combustor domain. From this figure, it can be observed that the incoming turbulent supersonic boundary layer encounters the sharp step which causes the boundary layer to separate and the flow turns downwards which leads to the formation of a Prandtl Meyer Expansion Fan (PMEF). A strong bow shock is caused when the airstream encounters the flow from the injector, with a small upstream separation bubble. The shock waves generated by the injected jet and the PMEFs at the step, together create a region of strong convection near the injector. The interaction of the strong bow shock with the fuel jet leads to the creation of baroclinic torque, which then leads to the formation of a counter-rotating vortex pair in the streamwise direction after the jet inlet. The incoming high speed air also creates a high momentum region over the jet which blocks the upwards penetration of the jet. This bends and elongates the jet in the streamwise direction, as seen in Fig. 13. After the jet passes through the convection dominated shock enhanced region, the shape of the jet is determined by the counter-rotating vortex pair. In the absence of any flow accelerating mechanism, the jet rises and diffuses laterally, while decaying in the streamwise direction, with the growing size of the counter-rotating vortices.

Fig. 14 shows the comparison of the P_{norm} isobars for all 3 cases on the mid X-Y plane of the combustor. It can be observed, particularly for Case A and B, that the bow shock impinges upon the PMEF and compresses it, causing a blockage of the incoming flow. More compression can be observed for the jet placed nearer to the step.

In Fig. 15 compares the mixture fraction contours, along with flow streamlines, on the mid X-Y plane of the combustor for the three cases. The size of the recirculation region increases with the distance of the injector from the step. In case C, as the injector is placed in the reattachment region, the jet encounters a boundary layer which creates an additional separation bubble, absent from the other cases, upstream to the separation bubble created by the injected jet.

4.0.2. Effect of streamwise vorticity

One of the mechanisms to augment mixing in a SCRAMJET engine is through shock-induced streamwise vorticity. The transverse sonic jet creates strong pressure gradients through its interaction with the bow and oblique shocks and results in creating a strong baroclinic torque. As seen in Eq. (1), this torque in turn creates streamwise vorticity in the flow field which serves to enhance mixing. To assess and quantify the creation of streamwise vorticity, the magnitude of the streamwise vorticity is computed over the Y-Z plane of the flow domain. This magnitude of the streamwise vorticity (Γ) is computed as the area integral of the total magnitude:

$$\Gamma(x) = \iint_{yz} \left| \frac{\partial v}{\partial z} - \frac{\partial w}{\partial y} \right| dydz \tag{27}$$

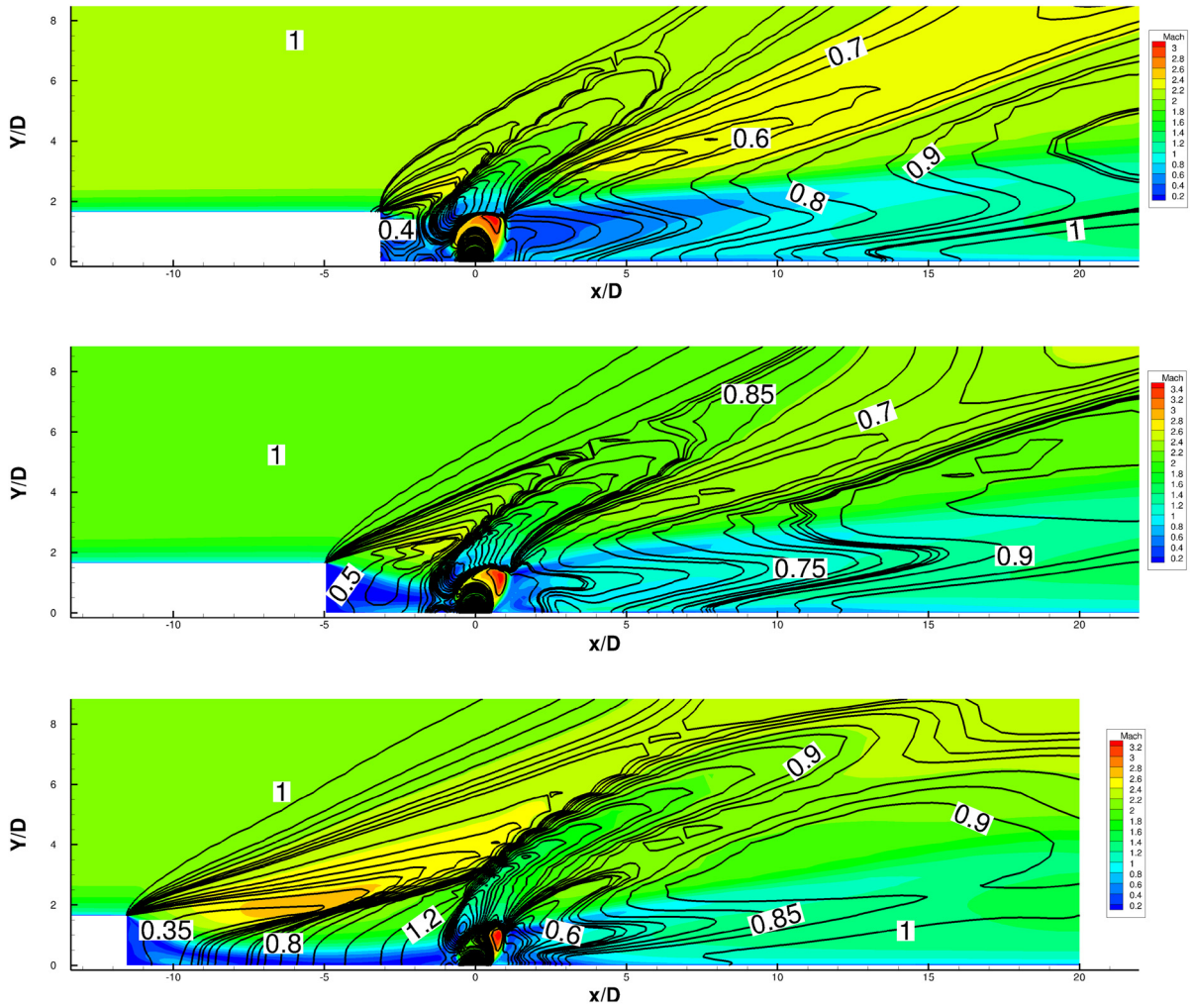

Fig. 14. Comparison of the center-plane P_{norm} isobars for Case A, B and C respectively (top to bottom).

across the entire Y-Z plane of the domain at various X locations downstream of the jet.

The variation of $\Gamma(x)$ for the three cases has been shown in Fig. 16 and has been compared with the supersonic flow (i.e. without injection) over the backward facing step which is referred to as the *baseline case* in the results presented from here onwards. It is worth mentioning that, due to the absence of bow shocks, the baseline case has the value of Γ as 0. However for the other 3 cases, a steep rise in $\Gamma(x)$ is observed. This rise begins just before the step and reaches its maximum just over the jet injection point and monotonically decreases further downstream. This is due to the strong pressure gradients created due by the presence of the Mach disk and barrel shocks. A higher peak value of $\Gamma(x)$ is observed when the injector is nearer to the step.

From Fig. 14, it can be seen that the PMEF from the step undergoes compression by the bow shock formed before the injected jet. This compression does not allow the jet to expand freely, resulting in a blockage effect. This interaction between the PMEF and the bow shock also creates the baroclinic torque which, in turn, creates streamwise vorticity. Jet location closer to the step results in more compression, a higher blockage effect, higher baroclinic torque and more vorticity. In case C, since the injector is situated farthest from the step, the compression of PMEF is least, which results in a lower increase in $\Gamma(x)$ as seen in the figure.

These results exhibit a complex dependence of streamwise vorticity on the flow field conditions such as the blockage effect and the bow shock strength and establish the role of the interaction of the jet and the streamwise flow in creating vorticity. Also evident is the influence of the recirculation zone after the step in determining the flow and mixing downstream of the jet. As the flow becomes more dominated by diffusion downstream of the injector, a monotonic decay of $\Gamma(x)$ is observed in Fig. 16, to reach seemingly asymptotic values in the far field around $x/D \geq 15$.

4.0.3. Mixing characteristics

As discussed, the mixing fraction ϕ is tracked in order to observe the mixing between the jet and the incoming flow. The jet penetration and spread boundaries which have been previously defined in Sec. 3.2 are shown in Fig. 17a and 17b respectively. The injected jet must penetrate the cross flow to increase mixing. It can be seen from Fig. 17a that the penetration downstream ($x/D < 8$) of the jet is highest for the case with the injector closest to the step, but further away ($x/D > 8$) the jet penetration is very similar for the three cases considered. The flow near the injector is characterized by the strong convective forces, which results in the observed steep rise in penetration height near the injector inlet as, seen in Fig. 17a. It can also be observed that between $x/D = 0$ and $x/D \approx 8$, the penetration boundary first increases and then decreases which correlates with the strong increase in $\Gamma(x)$ followed by its steep fall in the same regions.

Fig. 17b shows the spread of the injected jet into the Y-Z plane. A steep increase in the spread is observed in the region immediately downstream of the injector, but further away the spreading stops and the jet width becomes essentially constant. The over-

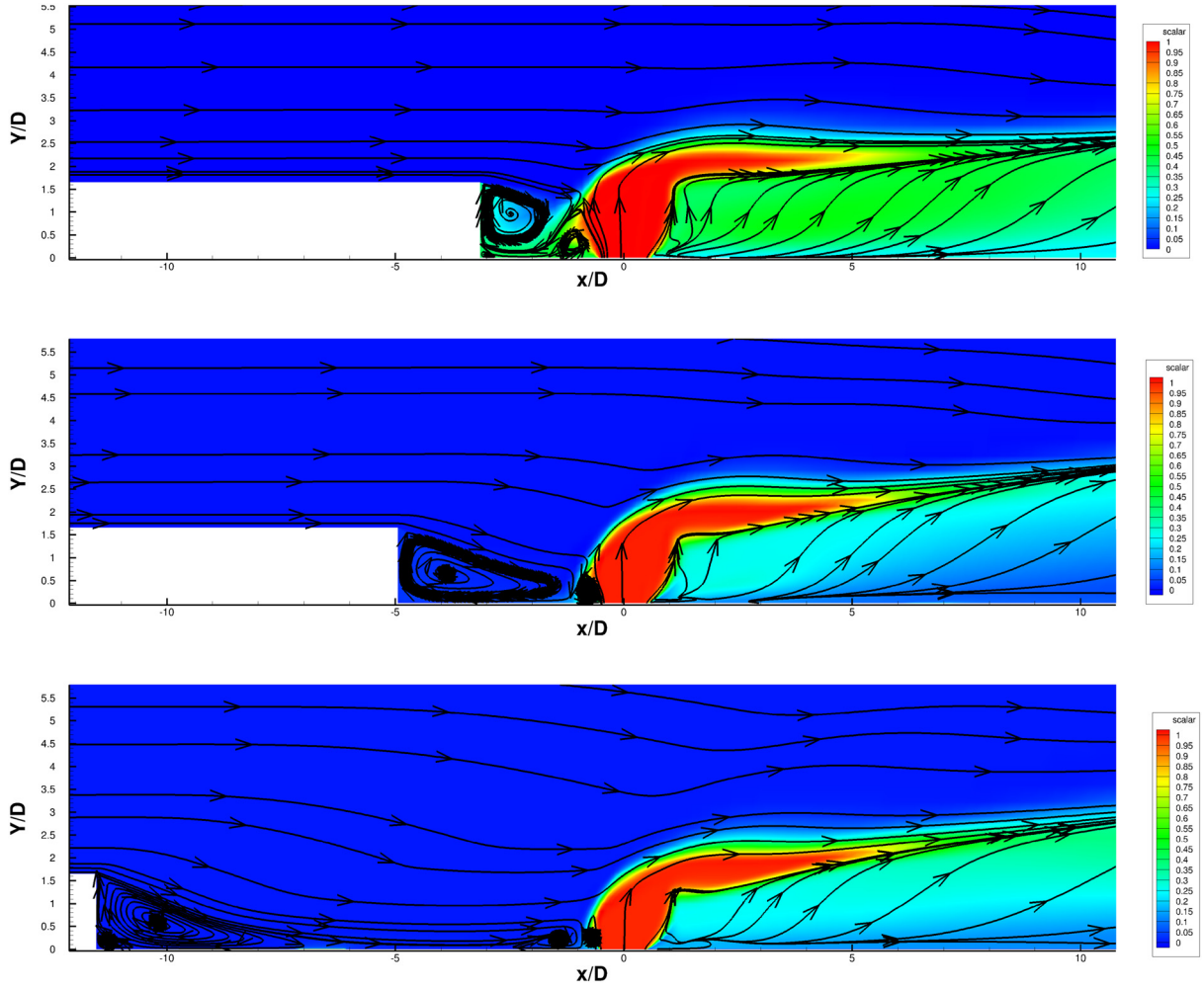

Fig. 15. Comparison of the center-plane mixture fraction contours with streamlines for Case A, B and C respectively.

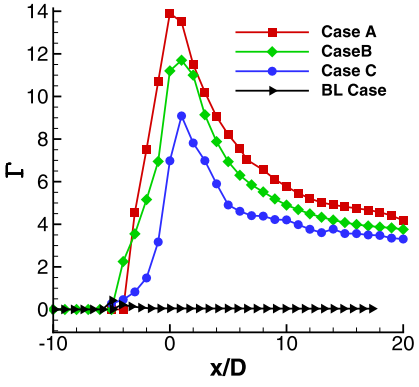

Fig. 16. Average magnitude of the streamwise vorticity in the Y-Z plane.

all spread of the jet is almost independent of the distance of the injector from the step, although case B gives a marginally higher spread compared to the other cases.

Fig. 17c shows the value of maximum mixing fraction of ϕ present in the jet. It can be presumed that a higher value of ϕ_{max} indicates poorer mixing. In the region beyond $x/D \approx 8$, there is an almost linear decay in the value of ϕ_{max}. Once again, there is little difference between three cases in this region, except that case A gives marginally better mixing, followed by case B and C.

Comparing the mixing characteristics from all the three cases, it can be seen that the mixing region becomes smaller, thicker and the rate of mixing decreases as the jet is placed away from the step, although further downstream the effect of the jet location is marginal. Fig. 17d shows the division of the flow into various regimes on the jet penetration graph for Case B. Region from A' to A, represents the flow preceding the injector. A sharp rise in the value of jet penetration between A and B represents the convection dominated region, which exists till $x/D \approx 3$. After the location B, the penetration boundary falls and then begins to rise at point C, which is located at $x/D \approx 8$. Beyond C the penetration boundary rises slowly in the diffusion dominated region till the end of graph at D.

An important point refers to the presence of scalar in the region preceding the jet inlet. From Fig. 17, it can be seen that some of the injected scalar is trapped in the recirculation zone and does not participate in mixing. This observation is also supported by Fig. 15. As the scalar represents the fuel stream, this means some of the fuel is trapped in the recirculation zone which acts as a flame holder in the actual SCRAMJET combustor for cases A and B. A small amount of fuel in this recirculation zone can aid in sustaining the flame in such high momentum flow. However, for case C, no scalar is present in the recirculation zone, because the injector is placed in the reattachment zone, which is quite far away from the recirculation zone created by the step. This would mean that if the jet is located in the reattachment region (case C), the combustor would require an alternate fuel feed to the flame holder.

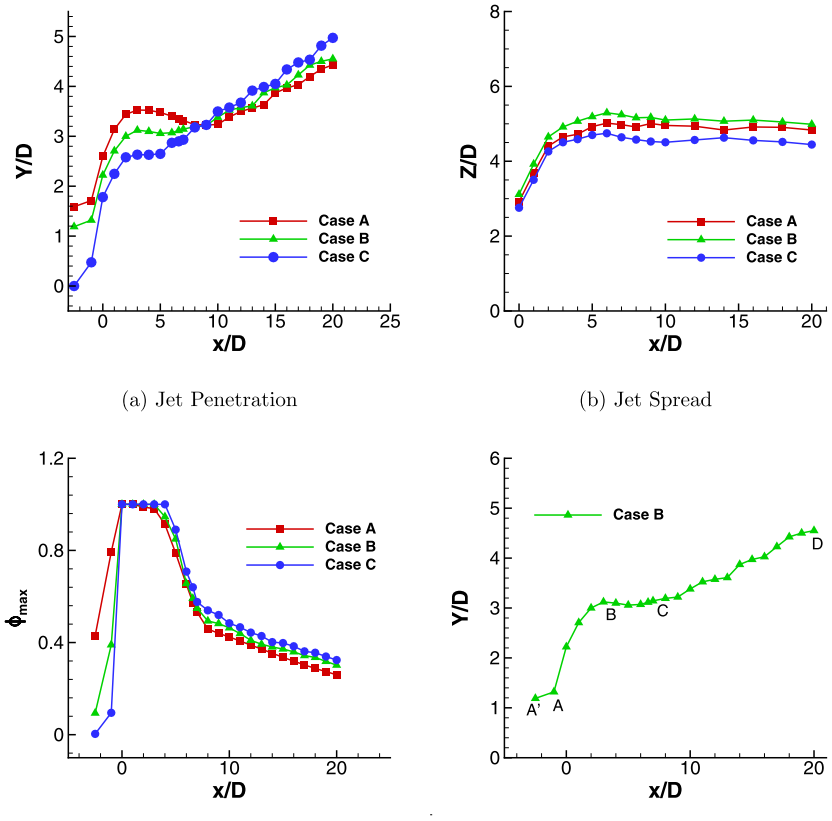

(a) Jet Penetration

(b) Jet Spread

(c) Maximum Mixture Fraction of scalar

(d) Flow regime description

Fig. 17. Mixing characteristics.

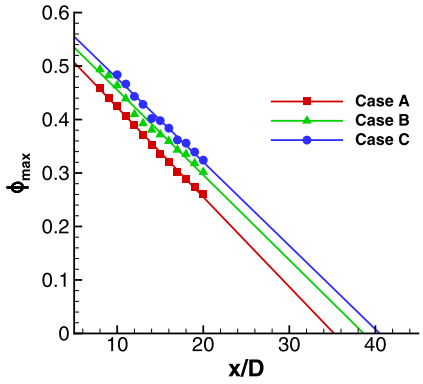

Fig. 18. Plot showing decay of ϕ_{max} after it has been reduced to half of its injected value.

4.0.4. Length of the combustor

The total length required for complete mixing of the jet with the incoming flow is estimated in this section. A complete mixing is said to have been achieved when the maximum scalar mass fraction (ϕ_{max}) in the mixing boundary becomes 0. In Fig. 17c, it can also be observed that in all the cases beyond $x/D \approx 8$, an absence of any flow accelerating mechanism leads to a linear decay the ϕ_{max}. The data from this region of from Fig. 17c is replotted in Fig. 18. A linear fit is introduced between the data points as shown in Fig. 18. The point where the linear fit intercepts the X-axis gives an estimated length required for complete mixing i.e. $\phi = 0$, under the admittedly strong assumption that the decay remains linear for the entire length. This intercept is the distance from the center of the injector. In order to obtain total length of the combustor (L_2), L_3 must be added to the intercept obtained for each case. It can be observed from the results from Fig. 18 that a longer combustor is required the farther away the jet is placed from the step. This conclusion seems reasonable, despite the strong assumption of linearity made to arrive at it.

4.0.5. Jet lift-off

Jet lift-off refers to the separation of the injectant jet from the lower wall downstream of the injection. The strong convection field near the injector and the counter-rotating vortices formed are responsible for the jet lift-off as seen in Fig. 19. The evolution of streamwise counter-rotating vortices (CRV) formed due to the baroclinic torque is also shown in Fig. 19. The figure consists of CRV formed at different locations in the combustor along the Y-Z plane, represented by contours of streamwise vorticity. These CRV have been shown along with the mixture fraction of the jet plume, which is represented by the dash-dot lines with the percentage values also marked in the figures. Fig. 19a, 19b and 19c represent the CRV present at $x/D = 0, 5, 10$ respectively.

As the jet exits the injector at $x/D = 0$ as shown in Fig. 19a, two CRV L and R, are formed by the baroclinic torque. It can be seen in the Fig. 19b that at $x/D = 5$ the 10% mixture contour has grown in size, and the two CRV have lifted off from the surface. It can also be seen that as the flow moves downstream, both vortices have moved significantly closer to each other as compared to Fig. 19a. Fig. 19c shows that, in the far-field, the jet plume has further grown in size, and the CRVs have also lifted off quite high from the bottom plate.

In Fig. 19c, we also see *another* counter-rotating vortex pair below the CRV. This is the *horse shoe* vortex pair commonly seen in the boundary layers in both incompressible and compressible flows. As the jet acts as a bluff body for the incoming cross flow, it leads to the creation of this horse-shoe vortex pair, which remains

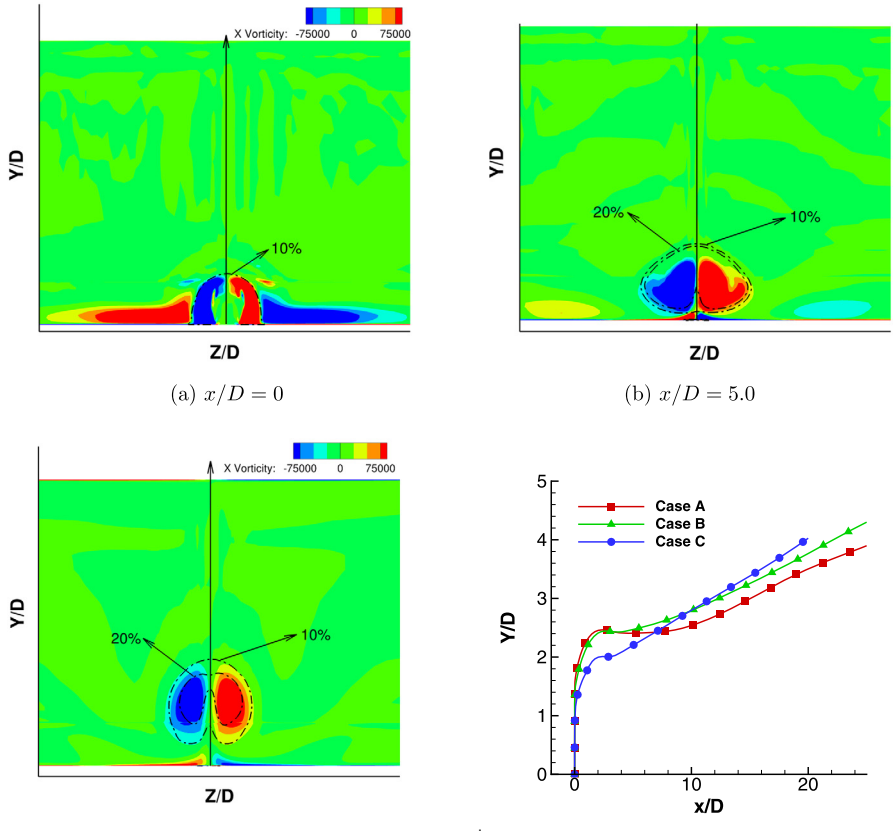

(a) $x/D = 0$ (b) $x/D = 5.0$

(c) $x/D = 10.0$ (d) Jet Liftoff from centre of the injector.

Fig. 19. Plots comparison of evolution of the streamwise counter-rotating vortices at different x/D planes in the flow field and comparison of jet-liftoff. The dashed lines are contours of mixture fraction ϕ.

attached to the wall surface. As the jet lifts off, the horse-shoe vortices move in to fill in the void in Fig. 19c. The further growth in size of the jet in the far field shows greater mixing in the far field due to diffusion, as also evident from Fig. 17c.

In order to compare this lift-off between different configurations, we have determined it by following a single streamtrace from the center point of the injector on the mid X-Y plane of the combustor. The lift-off height of the jet from the surface of the computational domain has been plotted in Fig. 19d, and shows that the jet lift-off closely follows the penetration boundary in Fig. 17.

Fig. 19d shows that almost parallel jet lift-off heights are achieved by Case A and B, with Case B somewhat higher than Case A in the diffusion dominated region. A higher lift-off slope is obtained in Case C in the same far-field region. Since this process is taking place in a confined domain, a very high lift-off may result in the mixing layer coming in contact with the upper walls of the combustor, thereby requiring a larger combustor for Case C.

4.0.6. Stagnation pressure loss

SCRAMJET configurations with transverse sonic jets produce substantial loss in stagnation pressure due to the interaction of the strong bow shocks produced by the jet with the incoming high speed flow. To generate more thrust, a higher exit velocity is needed. Hence lower stagnation pressure loss between the inlet and exit is desirable in the combustor. Therefore, even in cold flow calculations, the loss of stagnation pressure will reflect on the performance of the SCRAMJET engine. In order to quantify the loss in stagnation pressure on the basis of location of the jet, we define P_0 as the mass-flow-weighted average of stagnation pressure p_0 in the Y-Z plane:

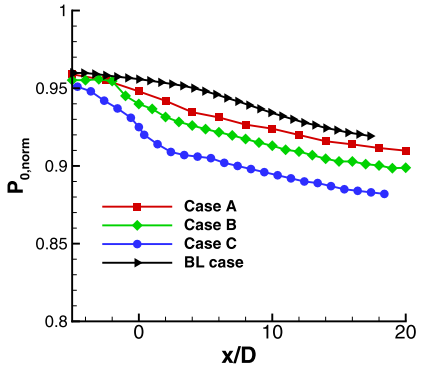

Fig. 20. Normalized stagnation Pressure distribution in Y-Z plane.

$$P_0(x) = \iint_{yz} p_0 \rho u \, dy \, dz \Big/ \iint_{yz} \rho u \, dy \, dz \tag{28}$$

subsequently normalized as $P_{0,norm}$ by dividing $P_0(x)$ with P_0 at the inlet. In Fig. 20, $P_{0,norm}$ is plotted in the Y-Z plane for all 3 cases and is compared with the results from the baseline case. A small loss in $P_{0,norm}$ values is observed even in the baseline case. With jet injection, a steep decrease in values of $P_{0,norm}$ in the immediate downstream of the injector ($x/D > 0$) is observed due to the presence of the bow shocks due to the injection. A higher loss in $P_{0,norm}$ shows presence of stronger shock strength. [In the region preceding the injector ($x/D < 0$), the values of $P_{0,norm}$ are unequal between all three cases due to the presence of the injector in different flow regimes.] A steady decrease in the value of $P_{0,norm}$ for all the cases can be attributed to the bow shocks that are formed in front of the injector, which is absent in the results

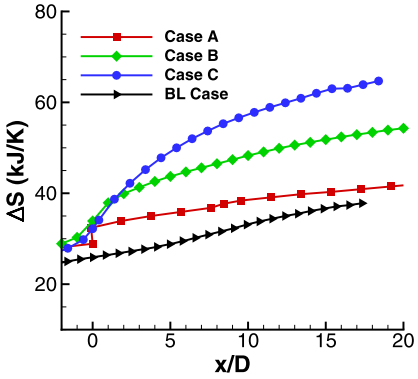

Fig. 21. ΔS distribution in Y-Z plane.

of the baseline case. The loss in $P_{0,norm}$ decreases as the injector is moved closer to the step. Also, higher loss in $P_{0,norm}$ exhibits presence of stronger shocks in system. Hence, it can also be concluded that the strength of the shocks from the injector become stronger as the jet is moved further from the step. In particular, the case C shows significant loss of stagnation pressure in comparison to the other two cases.

4.0.7. Entropy

An irreversible process leads to change in entropy of a system. Also, the rise in entropy represents the total amount of energy unavailable to do work. Hence a greater rise in entropy results in a less efficient system. Entropy increase (ΔS) in the SCRAMJET combustor rises primarily due to the mixing of the jet and air and due to presence of shocks in the system. The change in entropy in the computational domain at every cell center c is computed using Gibb's law as:

$$\Delta S_c = C_p\, ln(T_{norm}) - R\, ln(P_{norm}) \tag{29}$$

where the reference state is taken as the inlet condition. The entropy in the Y-Z plane is then evaluated as a mass flow weighted average:

$$\Delta S(x) = \iint_{yz} \Delta S_c \rho u\, dy\, dz \Big/ \iint_{yz} \rho u\, dy\, dz \tag{30}$$

Fig. 21 shows the average entropy change for all three cases is compared with the baseline case.

It is observed from the figure that ΔS of the system increases very significantly as the injector is moved further away from the step. This rise in ΔS can be attributed to presence of stronger shocks in the system. At first, the ΔS exhibits a sharp rise around the injector. The reason of this sudden rise can be traced to combination of presence of strong shocks and streamwise vorticity. As no or very weak shock structures are present in the region of decay of the mixing region (beyond $x/D \approx 8$), ΔS keeps increasing only due to the mixing and the graph becomes almost linear. The rise in ΔS for the baseline case is quite linear, as compared to the 3 cases due to absence of shocks and no mixing, as ΔS being primarily due to friction losses. This suggests that Case A is the most thermodynamic efficient followed by case B and C.

5. Conclusion

In order to optimize mixing and performance of a SCRAMJET engine, an optimal location is sought for placing the transverse sonic fuel jet in the incoming supersonic cross flow in the combustor, with a backward facing step acting as a flame holder. The study involves no combustion, as it has been suggested by previous work [15–17] that supersonic flow and combustion are quite decoupled in this situation, implying that even cold-flow optimization would be a good first approximation to the actual combustor problem. The results for the baseline case show that the flow field can be divided into three distinct flow regions downstream of the step, namely the recirculation created by the step, the reattachment stagnation point after the recirculation and a reattached region. A single jet is then placed in each of these three flow regions in separate simulations forming 3 cases for the study.

It is observed that the flow features are clearly influenced by the location of the jet. In order to quantify this influence and its effect on performance, various parameters were studied, for which results have been presented. First, the mixing for the three cases is quantified by calculating the effect of streamwise vorticity and mixing characteristics. In order to study mixing, a passive scalar injected along with the jet is tracked. It is observed that as the jet is placed nearer to the step, it results in higher spread and penetration of the injected jet, which leads to better mixing. By placing the jet nearer to the step, a higher average magnitude of streamwise vorticity is also observed. This leads to creating stronger convection forces around the injector, which in turn creates a higher blockage effect. The stronger convection aids in better mixing and in achieving higher penetration height. Using the mixing characteristics, the combustor length required for complete mixing is estimated. From the results, it can be seen that as the jet is moved away from the step, it leads to a requirement for a longer combustor length. It is also observed that as the jet location is moved nearer to the step, inside the recirculation region, the amount of fuel that gets trapped in the recirculation zone increases. This effectively increases the amount of fuel used for flame-holding, perhaps resulting in higher fuel losses.

In order to quantify the performance for all three cases, the stagnation pressure loss and rise in entropy of the system has been calculated. The loss in stagnation pressure increases with increase in distance of the injector from the step. This would lead to less exit velocity at the outlet, leading to loss of thrust and resulting in poor performance. Higher entropy rise leads to more unavailable work which results in a poorer performance.

We find in every criterion for mixing and performance, the Case C is the worst and Case A is the best, with Case B being intermediate. It can be safely concluded that placing the injector in the reattached region of the flow can be ruled out in an optimum design even if a separate fuel feed for the flame-holding can be designed. Further, from the analysis it can be concluded that the closer the injector is placed to the step, the better combustor design will be. But the injector placed too near to the step also traps too much fuel in the recirculation zone, which in turn decreases overall fuel efficiency. Small amounts of fuel in the recirculation region aids in flame holding, but large amounts will decrease the amount of fuel available for combustion.

Hence, the best location for the injector-without compromising on the combustor design, efficiency and losing only small amounts of fuel in the flame holder is-close to Case B. Therefore, the authors would recommend the stagnation point as the furthest optimal location for the injector. Whether the jet should be placed exactly ***at*** the stagnation point or somewhat ahead of it cannot be determined in a cold-flow study. It would require determination of whether the small amounts of fuel entering in the recirculation region is sufficient for flame holding. If not, the jet needs to be placed somewhat upstream of the stagnation point. As, in practice, the stagnation point would vary depending on the speed of inlet air, it would be safest to place the jet somewhat upstream of the design stagnation point. As the flow is supersonic, any jets downstream of the first one would not affect these conclusions. So, even when a series of jets are employed in the combustor, the authors

would recommend placing the first jet at or before the stagnation point.

Declaration of competing interest

This research did not receive any specific grant from funding agencies in public, commercial or not-for-profit sectors. The authors declare that they have no conflict of interest.

References

[1] D.W. Bogdanoff, Advanced injection and mixing techniques for scramjet combustors, J. Propuls. Power 10 (2) (1994) 183–190, https://doi.org/10.2514/3.23728.
[2] P. Roncioni, P. Natale, M. Marini, T. Langener, J. Steelant, Numerical simulations and performance assessment of a scramjet powered cruise vehicle at Mach 8, Aerosp. Sci. Technol. 42 (2015) 218–228, https://doi.org/10.1016/j.ast.2015.01.006.
[3] S. Chen, D. Zhao, RANS investigation of the effect of pulsed fuel injection on scramjet HyShot II engine, Aerosp. Sci. Technol. 84 (2019) 182–192, https://doi.org/10.1016/j.ast.2018.10.022.
[4] E.T. Curran, Scramjet engines: the first forty years, J. Propuls. Power 17 (6) (2001) 1138–1148, https://doi.org/10.2514/2.5875.
[5] J.M. Seiner, S. Dash, D. Kenzakowski, Historical survey on enhanced mixing in scramjet engines, J. Propuls. Power 17 (6) (2001) 1273–1286, https://doi.org/10.2514/2.5876.
[6] W. Huang, Z.-b. Du, L. Yan, R. Moradi, Flame propagation and stabilization in dual-mode scramjet combustors: a survey, Prog. Aerosp. Sci. 101 (2018) 13–30, https://doi.org/10.1016/j.paerosci.2018.06.003.
[7] W. Huang, Z.-b. Du, L. Yan, Z.-x. Xia, Supersonic mixing in airbreathing propulsion systems for hypersonic flights, Prog. Aerosp. Sci. 109 (2019), https://doi.org/10.1016/j.paerosci.2019.05.005.
[8] L.-q. Li, W. Huang, L. Yan, Z.-b. Du, M. Fang, Numerical investigation and optimization on the micro-ramp vortex generator within scramjet combustors with the transverse hydrogen jet, Aerosp. Sci. Technol. 84 (2019) 570–584, https://doi.org/10.1016/j.ast.2018.11.011.
[9] K. Arora, K. Chakravarthy, D. Chakraborty, Large eddy simulation of supersonic, compressible, turbulent mixing layers, Aerosp. Sci. Technol. 86 (2019) 592–598, https://doi.org/10.1016/j.ast.2019.01.034.
[10] S. Aso, S. Okuyama, Y. Ando, T. Fujimori, Two-dimensional and three-dimensional mixing flow fields in supersonic flow induced by injected secondary flows through traverse slot and circular nozzle, in: 31st Aerospace Sciences Meeting, AIAA, Reno, NV, U.S.A., 1993, p. 489.
[11] W. Huang, L. Yan, Progress in research on mixing techniques for transverse injection flow fields in supersonic crossflows, J. Zhejiang Univ. Sci. A 14 (8) (2013) 554–564, https://doi.org/10.1631/jzus.A1300096.
[12] W. Huang, Transverse jet in supersonic crossflows, Aerosp. Sci. Technol. 50 (2016) 183–195, https://doi.org/10.1016/j.ast.2016.01.001.
[13] V. Sharma, V. Eswaran, D. Chakraborty, Computational analysis of transverse sonic injection in supersonic crossflow using RANS models, Unpublished results.
[14] S.-H. Lee, Characteristics of dual transverse injection in scramjet combustor, part 1: mixing, J. Propuls. Power 22 (5) (2006) 1012–1019, https://doi.org/10.1016/j.expthermflusci.2013.08.022.
[15] V. Ton, A. Karagozian, F. Marble, S. Osher, B. Engquist, Numerical simulations of high-speed chemically reacting flow, Theor. Comput. Fluid Dyn. 6 (2–3) (1994) 161–179, https://doi.org/10.1007/BF00312347.
[16] S.-H. Lee, I.-S. Jeung, Y. Yoon, Computational investigation of shock-enhanced mixing and combustion, AIAA J. 35 (12) (1997) 1813–1820, https://doi.org/10.2514/2.56.
[17] S.-H. Lee, I.-S. Jeung, Y. Yoon, Computational investigation of shock-enhanced mixing: application to circular cross section combustor, AIAA J. 36 (11) (1998) 2055–2062, https://doi.org/10.2514/2.306.
[18] J.C. McDaniel, J. Raves, Laser-induced-fluorescence visualization of transverse gaseous injection in a nonreacting supersonic combustor, J. Propuls. Power 4 (6) (1988) 591–597, https://doi.org/10.2514/3.23105.
[19] J. Mcdaniel, D. Fletcher, R. Hartfield, S. Hollo, Transverse Injection Into Mach 2 Flow Behind a Rearward-Facing Step - A 3-D, Compressible Flow Test Case for Hypersonic Combustor CFD Validation, AIAA, 1991, p. 5071.
[20] A. Karagozian, K. Wang, A.-T. Le, O. Smith, Transverse gas jet injection behind a rearward-facing step, J. Propuls. Power 12 (6) (1996) 1129–1136, https://doi.org/10.2514/3.24153.
[21] D. Chakraborty, A. Roychowdhury, V. Ashok, P. Kumar, Numerical investigation of staged transverse sonic injection in Mach 2 stream in confined environment, Aeronaut. J. 107 (1078) (2003) 719–729, https://doi.org/10.1017/S0001924000013476.
[22] A. Sriram, D. Chakraborty, Numerical exploration of staged transverse injection into confined supersonic, Def. Sci. J. 61 (1) (2011) 3–11, https://doi.org/10.14429/dsj.61.20.
[23] T. Ukai, H. Zare-Behtash, E. Erdem, K.H. Lo, K. Kontis, S. Obayashi, Effectiveness of jet location on mixing characteristics inside a cavity in supersonic flow, Exp. Therm. Fluid Sci. 52 (2014) 59–67, https://doi.org/10.1016/j.expthermflusci.2013.08.022.
[24] W. Huang, Mixing enhancement strategies and their mechanisms in supersonic flows: a brief review, Acta Astronaut. 145 (2018) 492–500, https://doi.org/10.1016/j.actaastro.2018.02.022.
[25] J.M. Weiss, W.A. Smith, Preconditioning applied to variable and constant density flows, AIAA J. 33 (11) (1995) 2050–2057, https://doi.org/10.2514/3.12946.
[26] F.M. White, I. Corfield, Viscous Fluid Flow, vol. 3, McGraw-Hill, New York, 2006, pp. 67–73, Ch. 2.
[27] J.M. Weiss, J.P. Maruszewski, W.A. Smith, Implicit solution of preconditioned Navier-Stokes equations using algebraic multigrid, AIAA J. 37 (1) (1999) 29–36, https://doi.org/10.2514/2.689.
[28] P.L. Roe, Approximate Riemann solvers, parameter vectors, and difference schemes, J. Comput. Phys. 43 (2) (1981) 357–372, https://doi.org/10.1016/0021-9991(81)90128-5.
[29] V. Venkatakrishnan, On the accuracy of limiters and convergence to steady state solutions, in: 31st Aerospace Sciences Meeting, AIAA, Reno, NV, U.S.A., 1993, p. 880.
[30] V. Venkatakrishnan, Convergence to steady state solutions of the Euler equations on unstructured grids with limiters, J. Comput. Phys. 118 (1) (1995) 120–130, https://doi.org/10.1006/jcph.1995.1084.
[31] W. Huang, W.-d. Liu, S.-b. Li, Z.-x. Xia, J. Liu, Z.-g. Wang, Influences of the turbulence model and the slot width on the transverse slot injection flow field in supersonic flows, Acta Astronaut. 73 (2012) 1–9, https://doi.org/10.1016/j.actaastro.2011.12.003.
[32] M. Ou, L. Yan, W. Huang, S.-b. Li, L.-q. Li, Detailed parametric investigations on drag and heat flux reduction induced by a combinational spike and opposing jet concept in hypersonic flows, Int. J. Heat Mass Transf. 126 (2018) 10–31.
[33] F.R. Menter, Two-equation eddy-viscosity turbulence models for engineering applications, AIAA J. 32 (8) (1994) 1598–1605, https://doi.org/10.2514/3.12149.
[34] P.J. Roache, Perspective: a method for uniform reporting of grid refinement studies, J. Fluids Eng. 116 (3) (1994), https://doi.org/10.1115/1.2910291.